An Immunotolerant HER-2/*neu* Transgenic Mouse Model of Metastatic Breast Cancer

Hong Song,[1] Karineh Shahverdi,[1] David L. Huso,[5] Yuchuan Wang,[4] James J. Fox,[2] Robert F. Hobbs,[1] Barjor Gimi,[3] Kathleen L. Gabrielson,[5] Martin G. Pomper,[2] Benjamin M. Tsui,[4] Zaver Bhujwalla,[3] R. Todd Reilly,[6] and George Sgouros[1]

Abstract

Purpose: Animal models of breast cancer metastases that recapitulate the pattern of metastatic progression seen in patients are lacking; metastatic breast cancer models do not currently exist for evaluation of immune-mediated therapies. We have developed and characterized a preclinical model for the evaluation of immune-mediated metastatic breast cancer therapies.

Experimental Design: The NT2.5 mammary tumor cell line was injected into the left cardiac ventricle of immunotolerant transgenic *neu*-N mice and athymic *nu*/*nu* mice. Metastatic progression was monitored by bioluminescent, small-animal magnetic resonance imaging, positron emission tomography, single-photon emission computed tomography/computed tomography imaging, and also by histopathology. Antigen expression in normal organs and tumor metastases was evaluated by Western blot analysis and flow cytometry.

Results: Left cardiac ventricle injection of NT2.5 cells yielded widespread metastases in bones, liver, and spleen. Three to four weeks after injection, mice exhibited hind limb paralysis and occasional abdominal enlargement. Bioluminescence imaging of metastatic progression was successful in nude mice but the bioluminescent cells were rejected in immunocompetent mice. Other imaging modalities allowed successful imaging of nonbioluminescent cells. Small-animal positron emission tomography imaging allowed visualization of disease, *in vivo*, in the bones and liver. Magnetic resonance imaging revealed initial dissemination of the tumor cells to the bone marrow. Small-animal single-photon emission computed tomography/computed tomography imaging identified metastatic bone lesions targeted by a radiolabeled antibody.

Conclusion: The model closely recapitulates the pattern of metastatic spread in breast cancer. This immunotolerant metastatic model is a novel addition to existing breast cancer models and coupling the model with *in vivo* imaging greatly facilitates the evaluation of targeted immunotherapies of metastasis.

Treatment failure in cancer is largely the failure to control or eliminate metastatic dissemination. Breast cancer patients with distant metastases at diagnosis have a diasheartening 26.7% five-year survival rate (1). At autopsy, 50% of breast cancer patients show metastatic disease in bone, lung, liver, lymph nodes, or pleura (2, 3). Multiple sites of disseminated disease are also commonly observed in ~45% of patients (3). Agents that target breast cancer must therefore be tested against animal models that recapitulate the metastatic dissemination seen in breast cancer patients.

Existing genetic murine models were developed to study tumorigenesis, such as MMTV-HER-2/*neu* (4), MMTV-PyV mT (5), WAP-*p53* (6), and MMTV-TGF-β (7). Most of these models form spontaneous mammary tumors as well as pulmonary and lymph node metastases, but rarely bone or liver metastases. Tumors induced by chemical carcinogens, such as *N*-ethyl-*N*-nitrosourea, do not progress to widespread metastases (8). Orthotopic transplantation of human tumors into severe combined immunodeficient mice has been shown to induce widespread metastases, including bone, lung, and liver metastases (9–11). I.v. or intracardiac injection of human xenograft tumor cells in severe combined immunodeficient mice has also been used to induce lung metastases or bone metastases and has been used to determine genetic profiles associated with cell metastatic potentials (12). These xenograft models are very useful in elucidating the genetic root of tumor cell metastatic behavior.

In the investigation of targeted immunotherapies, however, these models are suboptimal because the human tumor

Authors' Affiliations: Divisions of [1]Nuclear Medicine, [2]Neuroradiology, [3]Magnetic Resonance Research, and [4]Medical Imaging Physics, [5]Russell H. Morgan Department of Radiology and Radiological Science, Department of Molecular and Comparative Pathobiology, and [6]Sydney Kimmel Cancer Center, School of Medicine, Johns Hopkins University, Baltimore, Maryland

Received 10/18/07; revised 3/13/08; accepted 4/8/08.

Grant support: NIH/National Cancer Institute grant R01 CA113797 (G. Sgouros), U24 CA92871 (M.G. Pomper), and Department of Defense Fellowship BC044176 (H. Song).

The costs of publication of this article were defrayed in part by the payment of page charges. This article must therefore be hereby marked *advertisement* in accordance with 18 U.S.C. Section 1734 solely to indicate this fact.

Requests for reprints: George Sgouros, Johns Hopkins University School of Medicine, Cancer Research Building II, Room 4M.61, 1550 Orleans Street, Baltimore, MD 21231. Phone: 410-614-0116; Fax: 413-487-3753; E-mail: gsgouros@jhmi.edu.

doi:10.1158/1078-0432.CCR-07-4672

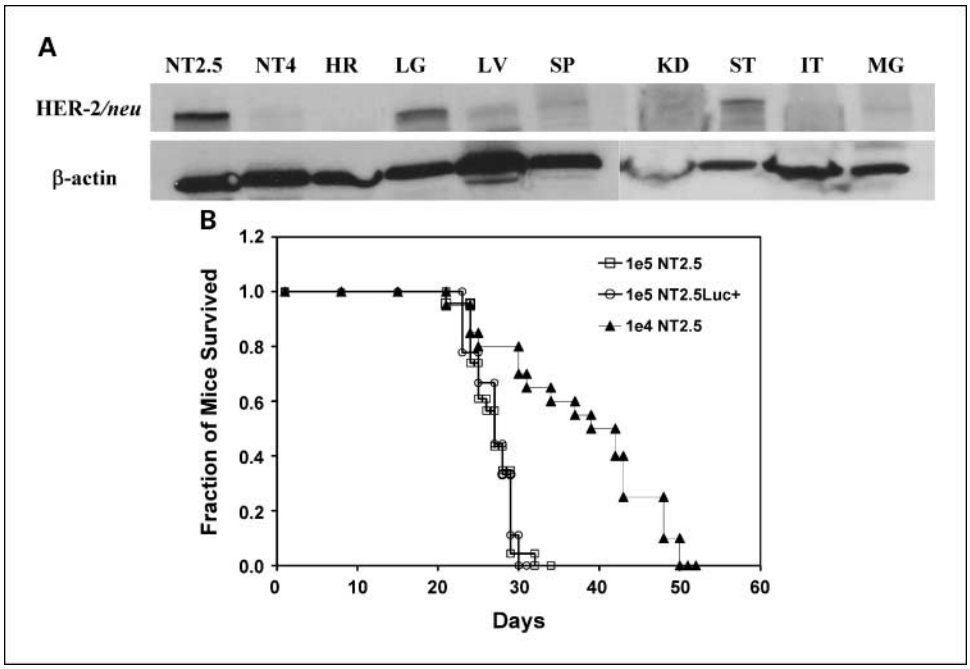

Fig. 1. *A,* Western blot of rat HER-2/*neu* expression on normal organs of *neu*-N transgenic mice. HER-2/neu positive NT2.5 and negative NT4 cells are used as control. HR, heart; LG, lung; LV, liver; SP, spleen; KD, kidney; ST, stomach; IT, intestine; MG, mammary gland. *B,* Kaplan-Meier survival curve of *neu*-N transgenic mice following left cardiac ventricular injection of 1×10^5, 1×10^4 NT2.5 cells in *neu*-N mice and 1×10^5 NT2.5Luc+ cells in nude mice. Median survival time was 27, 37.6, and 26.8 d, respectively.

xenografts exclusively express the targeted markers; this is not typically the case in clinical studies. More importantly, the immune system has been shown to be actively involved in both metastatic tumor killing through antibody-dependent cell-mediated cytotoxicity and metastases progression through immune editing and tumor escape of immune surveillance (13). Metastases in these immunodeficient mice, therefore, cannot faithfully mimic the complex tumor microenvironment due to lack of immune cell involvement. Bioluminescence- and fluorescence-based *in vivo* imaging has been widely used to monitor metastatic progression and drug response in mouse models (14, 15). The presence of foreign genes products, such as luciferase and green fluorescent protein, however, will induce host immune response in immunocompetent mice that complicates evaluation of response from immunotherapy.

In this study, we describe and characterize a mouse model of widespread metastatic dissemination, including liver and osteolytic bone metastases from an endogenously derived, rat HER-2/*neu*–expressing mammary carcinoma cell line. The model is based on the immunocompetent *neu*-N transgenic mouse model that was developed by Guy et al. (4) and expresses nontransforming rat *neu* cDNA under the control of a mammary specific MMTV enhancer. The *neu*-N model expressing wild-type *neu* has been extensively studied to dissect the *neu* tyrosine kinase–mediated signaling pathways in tumorigenesis and has helped identify the key mutation that activates the *neu* oncogene (16, 17). Observing the stochastic appearance and multistep induction of mammary tumors in the *neu*-N model, Reilly et al. (18) hypothesized and showed the immunotolerance to *neu* in this *neu*-N model. The *neu*-N model has since been used to study the mechanism of peripheral tolerance and possible therapeutic approaches to overcome such tolerance (19, 20). Using this established immunotolerant transgenic mouse model, we injected endogenously derived mammary carcinoma cells through the left cardiac ventricle and these *neu*-N mice developed widespread metastases to the bone marrow, liver, and spleen, leading to animal death after ~4 weeks of disease progression. To assess the level of cross-reactivity and potential normal organ toxicity following targeted therapy, the normal tissue expression of HER-2/*neu* was measured. To characterize metastatic progression, we transfected the syngeneic cell line with luciferase and found that metastatic progression of transfected cells was very slow in the immunocompetent *neu*-N mice; the same cells led to rapid metastatic dissemination in immunodeficient nude mice. Metastatic progression was instead characterized, *in vivo*, by imaging using magnetic resonance imaging (MRI), small-animal positron emission tomography (PET), and small-animal single-photon emission computed tomography/computed tomography (SPECT/CT; refs. 21, 22).

This immunotolerant metastatic mouse model is a useful addition to existing metastatic animal models and can serve as a relevant preclinical model for studying targeted radionuclide therapy and other active and passive immunotherapies.

Materials and Methods

Mice, cell lines, and mAbs. Rat HER-2/*neu* transgenic mice (*neu*-N; ref. 4), at 6 to 8 wk of age, were obtained from Harlan Bioproducts for Science, Inc. All animal experiments were approved by the Animal Care and Use Committee of The Johns Hopkins University School of Medicine (Baltimore, MD). The rat HER-2/*neu*–expressing mouse mammary tumor cell line, NT2.5, was established from spontaneous mammary tumors in female *neu*-N mice (18). A cell line (NT4) that does not express HER-2/*neu* was derived similarly. The NT lines are grown in RPMI containing 20% fetal bovine serum, 0.5% penicillin/streptomycin (Invitrogen), 1% L-glutamine, 1% nonessential amino acids, 1% sodium pyruvate, 0.02% gentamicin, and 0.2% insulin (Sigma) and maintained at 37°C in 5% CO_2. The hybridoma cell line for mouse anti-rat HER-2/*neu* monoclonal antibody (mAb), 7.16.4, was kindly provided by Dr. M. Greene (University of Pennsylvania, Philadelphia, PA). The 7.16.4 mAb collected from ascites of athymic

mice was purified by a HiTrap protein G column (GE Healthcare Biosciences), using a Biologic LP purification system (Bio-Rad), and dialyzed into PBS using Centricon YM-10 filter units (Millipore). Normal organs from the *neu*-N mice were harvested and homogenized in radioimmunoprecipitation assay buffer on ice and the expression of HER-2/*neu* was determined with Western blot using anti-rat-HER-2/*neu* Ab1 polyclonal antibody (Calbiochem) and anti-mouse β-actin mAb (Cell Signaling Technology) as loading control.

Determination of stability, binding affinity, number of binding sites, and antigen-mAb complex internalization. The 7.16.4 mAb was labeled with ^{111}In (MDS Nordion) following a published procedure (23). ^{111}In-7.16.4 was diluted 10 times in PBS and fetal bovine serum and incubated at 37°C and 4°C, respectively, for both diluents. Stability of the construct at 24, 48, 72, and 96 h after labeling was determined by instant TLC. ^{111}In-7.16.4 in serial increments of concentration (from 0.01 to 10 μg/mL) was incubated with NT2.5 cells (1.0×10^6) for 1 h on ice and the bound and unbound fraction of the construct was determined with a γ-scintillation counter (CompuGamma CS, Pharmacia) following three washes with PBS. The equilibrium binding curve of bound/free mAb versus bound mAb concentration was fitted and the number of binding sites, B_{max}, and binding affinity constant, K_D, were calculated. To determine the rate of internalization, the ^{111}In-7.16.4 construct was incubated with NT2.5 cells on ice and at 5, 30, 60, 120, 240, 360, and 1,440 min; incubation was terminated and the surface-bound mAb was

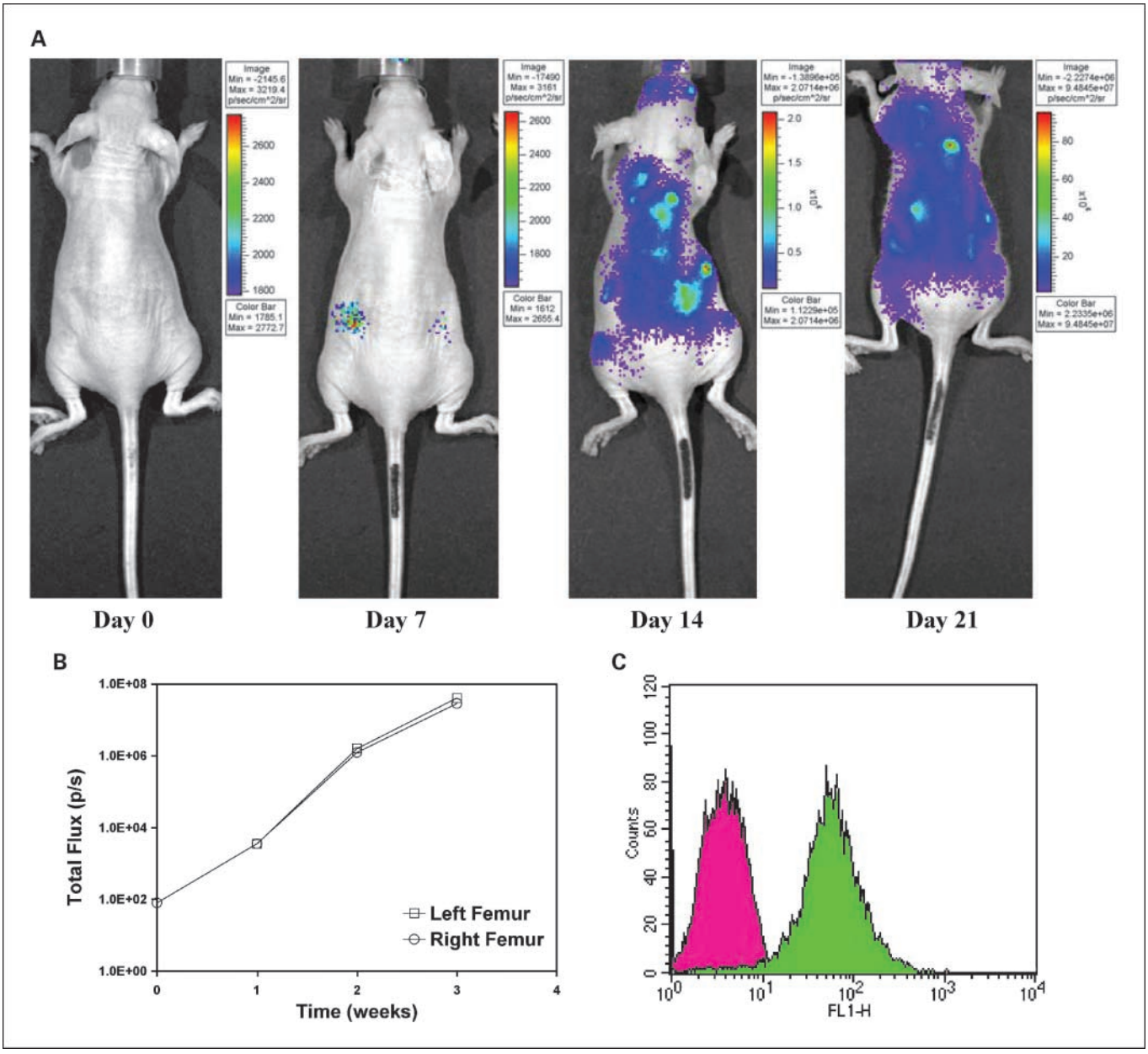

Fig. 2. Bioluminescence imaging of metastatic progression following left cardiac ventricular injection of 1×10^5 NT2.5Luc+ cells in nude mice. *A,* mice were imaged with the IVIS 200 imaging system at days 0, 7, 14, and 21 after tumor cell injection. *B,* a circular region of interest with fixed area was drawn around the left and right femoral-tibial joint area near the femoral-tibial joints and total photon flux per second was quantified over the imaged period. *C,* flow cytometric analysis of HER-2/*neu* expression on cells harvested from distal femur of the femoral-tibial joint area of imaged mice. Cells were selected for *neo* resistance. Unstained NT2.5 cells were used as a control.

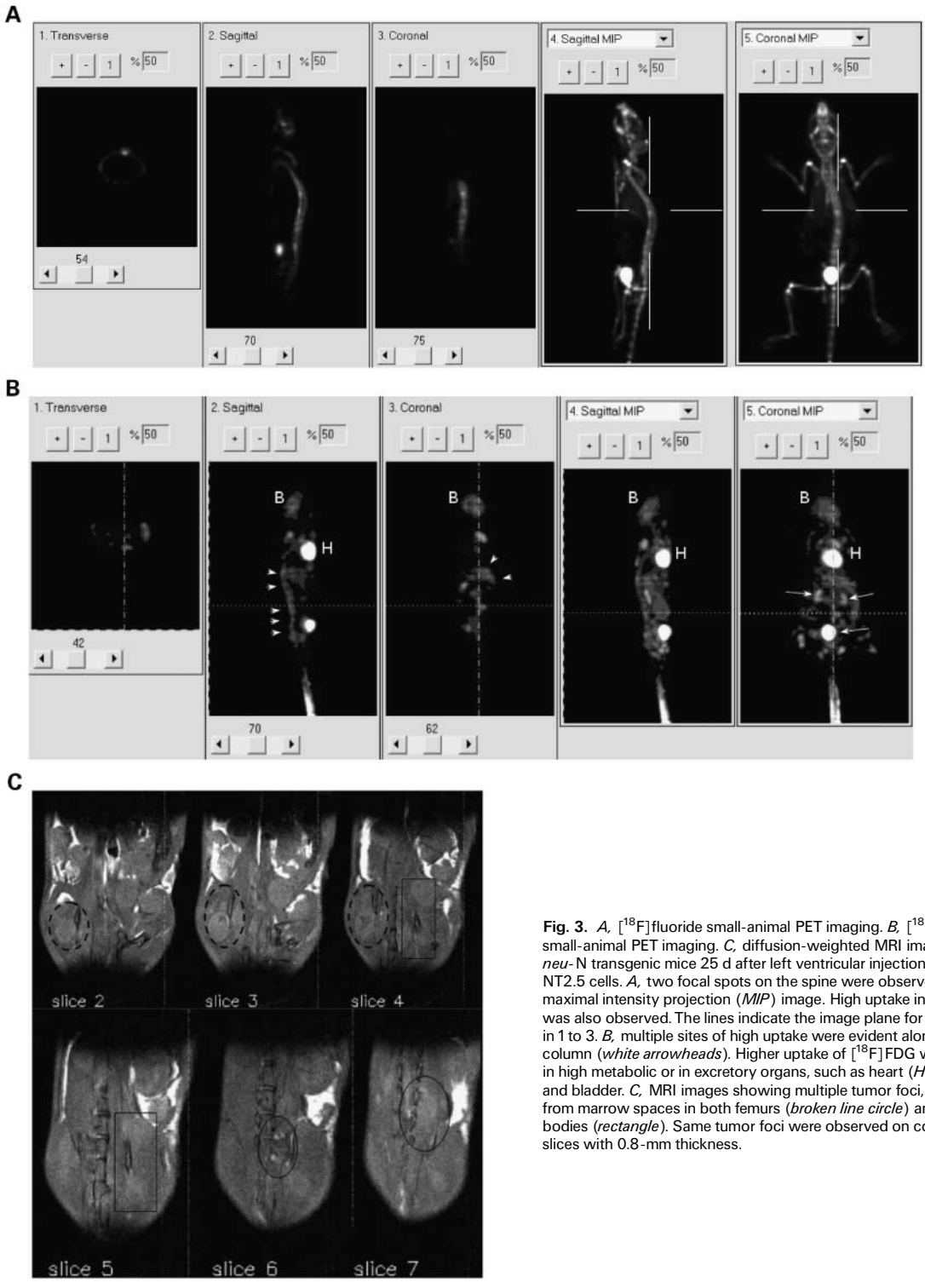

Fig. 3. *A,* [^{18}F]fluoride small-animal PET imaging. *B,* [^{18}F]FDG small-animal PET imaging. *C,* diffusion-weighted MRI imaging of *neu*-N transgenic mice 25 d after left ventricular injection of 1×10^5 NT2.5 cells. *A,* two focal spots on the spine were observed on the maximal intensity projection (*MIP*) image. High uptake in the bladder was also observed. The lines indicate the image plane for the sections in 1 to 3. *B,* multiple sites of high uptake were evident along the spinal column (*white arrowheads*). Higher uptake of [^{18}F]FDG was also seen in high metabolic or in excretory organs, such as heart (*H*), brain (*B*), and bladder. *C,* MRI images showing multiple tumor foci, emanating from marrow spaces in both femurs (*broken line circle*) and vertebral bodies (*rectangle*). Same tumor foci were observed on contiguous slices with 0.8-mm thickness.

stripped with 150 mmol/L NaCl/50 mmol/L glycine (pH 2.0; Sigma) for 10 min; and the internalized fraction was counted by γ-scintillation counter following three washes with PBS.

Left cardiac ventricular injection. *neu*-N mice, 6 to 8 wk of age, were anesthetized with a ketamine (90 mg/kg) and xylazine (10 mg/kg) mixture. NT2.5 cells (1.0×10^5) suspended in 100 μL cold PBS were injected into the left cardiac ventricle of *neu*-N mice following a published procedure (24). Successful injection was indicated by a pulsatile bright red blood into the 26-1/2G needle fitted with a 1.0-cm tuberculin syringe; successful injection was also confirmed, retrospectively, by the lack of abnormal tumor mass growth in the pleural cavity 3 wk after injection.

Bioluminescence imaging. The NT2.5 cells were cotransfected with 0.5 mg empty pcDNA3.1+ (Invitrogen) and 3.0 mg pGL3-Luc reporter vector (Promega) using 3 μL FuGene6 transfection reagent (Roche) in 50 μL Opti-MEM medium (Invitrogen). *In vitro* and *in vivo* selection of the transfected clones was done with an IVIS 200 Imaging System (Xenogen). Clones with strong bioluminescence signals (50 μg/mL luciferin-EF, Promega) were expanded and injected s.c. in nude mice for *in vivo* selection. Clones with the ability to form tumors were used for left cardiac ventricular injection. Metastatic disease progression in nude mice was followed weekly following left cardiac ventricular injection. Ten minutes before imaging, mice were anesthetized with 2.5% isoflurane (Abbott Laboratory) and injected i.p. with 50 mg/kg luciferin-EF. Imaging acquisition time ranged from 0.5 s to 1 min depending on the intensity of the bioluminescence signal. Images were analyzed and quantified with Living Image 3D software (Xenogen).

Small-animal **in vivo** *MRI, positron emission tomography, and SPECT/CT imaging.* Three weeks after left cardiac ventricular injection, mice were imaged by MRI, small-animal positron emission tomography (PET), and small-animal SPECT/CT. Mice were anesthetized with 2.5% isofluorane and kept under 1.0% isofluorane anesthesia throughout all imaging procedures. [^{18}F]FDG and [^{18}F]fluoride PET imaging was used to examine metastatic tumor cell induced metabolic and skeletal changes, respectively. Images were acquired with three bed positions (10 min per bed position for a total of 30 min) and an axial resolution of 1.2 mm using a GE Explore Vista dedicated small-animal PET scanner (GE Healthcare).

Diffusion-weighted MR images were acquired with a 4.7-T animal MR scanner (Avance, Brunker Biospin). A 2-cm RF coil built in-house was positioned around the abdominal part of the mouse that also encompasses the distal femur. Twelve slices, each 0.8-mm thick, were acquired over 20 min. All images were acquired with respiratory gating.

Small-animal SPECT/CT imaging of metastatic disease using the ^{111}In-labeled anti–HER-2/*neu* mAb 7.16.4 was also done. Mice bearing metastatic disease were injected i.v. with 200 μCi, at a specific activity of ~10 mCi/mg and imaged with an X-SPECT scanner (Gamma Medica) at 1, 24, and 48 h postinjection. SPECT images were reconstructed and registered with CT images acquired immediately after the end of SPECT imaging using a commercially available software package. The radioactivity concentration in metastatic lesions in the bone marrow of the distal femur near the femoral-tibial joint at three time points after tracer injection was quantified. An insulin syringe with defined geometry (5.0 cm in length and 0.36 cm in diameter with a total volume of 500 μL) was used, and known activity of $^{111}InCl_3$ (~10 μCi) was imaged and used as a reference for quantification of radioactivity.

Histopathology, immunohistopathology, and flow cytometry. Mice undergoing both bioluminescence imaging and radiological imaging were sacrificed after the last time point of the study. Femurs, tibia, lumbar and sacral regions of the spine, liver, spleen, lung, kidney, and heart were harvested and fixed in 10% formalin (Sigma) and embedded in paraffin, sectioned, and stained by H&E. Cells from the bone marrows of femur and tibia were flushed and harvested using a 26-1/2G syringe filled with PBS. Bone marrow cells from nude mice injected with luciferase-transfected NT2.5 cells were cultured and selected with a medium containing geneticin (Invitrogen). Bone marrow cells from *neu*-N mice injected with parental NT2.5 cells were cultured and propagated thrice using a 1:10 split ratio. Cell clones grown from both cultures were then stained with anti–HER-2/*neu* (7.16.4) and analyzed using FACSCalibur cytometer with CellQuest Pro software (BD Bioscience).

Results

*Characterization of rat HER-2/***neu** *and CXCR4 expression by NT2.5 mouse breast cancer cell line.* The majority (>99%) of NT2.5 cells stained positive for rat HER-2/*neu* on the surface as determined by immunofluorescence staining and flow cytometry. Both quantitative flow cytometry and Scatchard analysis found ~1.5 ± 0.1 × 10^5 rat HER-2/*neu* receptors on the surface of NT2.5 cells. The negative control cell line NT4 showed no staining and very low surface receptor expression (<1,000 receptors per cell). Using 7.16.4, an anti-rat HER-2/*neu* mAb, in the Scatchard analysis, the affinity constant was calculated as K_D = 2.1 $(nmol/L)^{-1}$. We also surveyed the expression of CXCR4, a chemokine receptor previously reported to be involved in breast cancer metastasis to bone, and found expression on ~17.3% of the NT2.5 cells. Rat HER-2/*neu* was also expressed on normal organs of *neu*-N mice as determined by Western blot. High expression was observed on the lungs and stomach, and low expression was found in the liver, spleen, and mammary gland. No expression was found on cells of the heart, kidneys, and intestines (Fig. 1A).

Metastasis progression following left cardiac ventricular injection of NT2.5 cells in **neu-N** *mice.* Three weeks (21 days) following left cardiac ventricular injection of 1.0 × 10^5 NT2.5 cells in *neu*-N mice, mice started to show symptoms of weight loss (~5-10% within 2-3 days), hind limb paralysis, and enlarged abdomen (confirmed to be due to ascite fluid accumulation). Kaplan-Meier survival curves following left cardiac ventricular injection of 1.0 × 10^5 (n = 23) or 1.0 × 10^4 (n = 20) NT2.5 cells in *neu*-N mice and 1.0 × 10^5 luciferase-transfected NT2.5 cells in nude mice (n = 9) are shown in Fig. 1. The median survival time was 27.0 and 37.6 days, respectively, for 1.0 × 10^5 and 1.0 × 10^4 NT2.5 cells in *neu*-N mice and 26.8 days for 1.0 × 10^5 luciferase-transfected NT2.5 cells in nude mice. No significant difference in survival time was observed for *neu*-N mice injected with NT2.5 cells and nude mice injected with luciferase-transfected NT2.5 cells (P = 0.44), whereas injection of one tenth of 1.0 × 10^5 NT2.5 cells significantly improved survival in *neu*-N mice (P < 0.001).

Bioluminescence imaging of metastasis progression. Metastatic progression in nude mice is shown with bioluminescence imaging on the first day, and 1, 2, and 3 weeks following left cardiac ventricular injection (Fig. 2A). Widespread metastases were observed at later stages of progression, accompanied by hind limb paralysis. There was very rapid progression from the 1- to 2-week period as quantification of the distal femur near the femoral-tibial joint areas confirmed that total photon flux increased from 3.46 × 10^3 and 3.54 × 10^3 photon/s to 1.58 × 10^6 and 1.23 × 10^6 photon/s for the right and left femur joint areas, respectively (Fig. 2B). Flow cytometry for HER-2/*neu* expression of luciferase-transfected cells harvested from the distal femur of the femoral-tibial joint is depicted in Fig. 2C.

However, slow to no metastatic progression was observed by bioluminescence imaging in *neu*-N mice 3 weeks after left cardiac ventricular injection (n = 3, data not shown). All mice remained viable during the period of monitoring (2 months). That was probably due to immune rejection of luciferase-transfected cells by the immunocompetent *neu*-N mice. Thus, small-animal imaging, such as MRI, small-animal SPECT/CT, and small-animal PET was assessed as a feasible approach to imaging metastatic progression in these immunocompetent animals.

Small-animal imaging, **in vivo**, *of metastatic progression by MRI, small-animal PET, and small animal SPECT/CT.* [^{18}F]fluoride and [^{18}F]FDG small-animal PET images are shown in Fig. 3A and B. The [^{18}F]fluoride small-animal

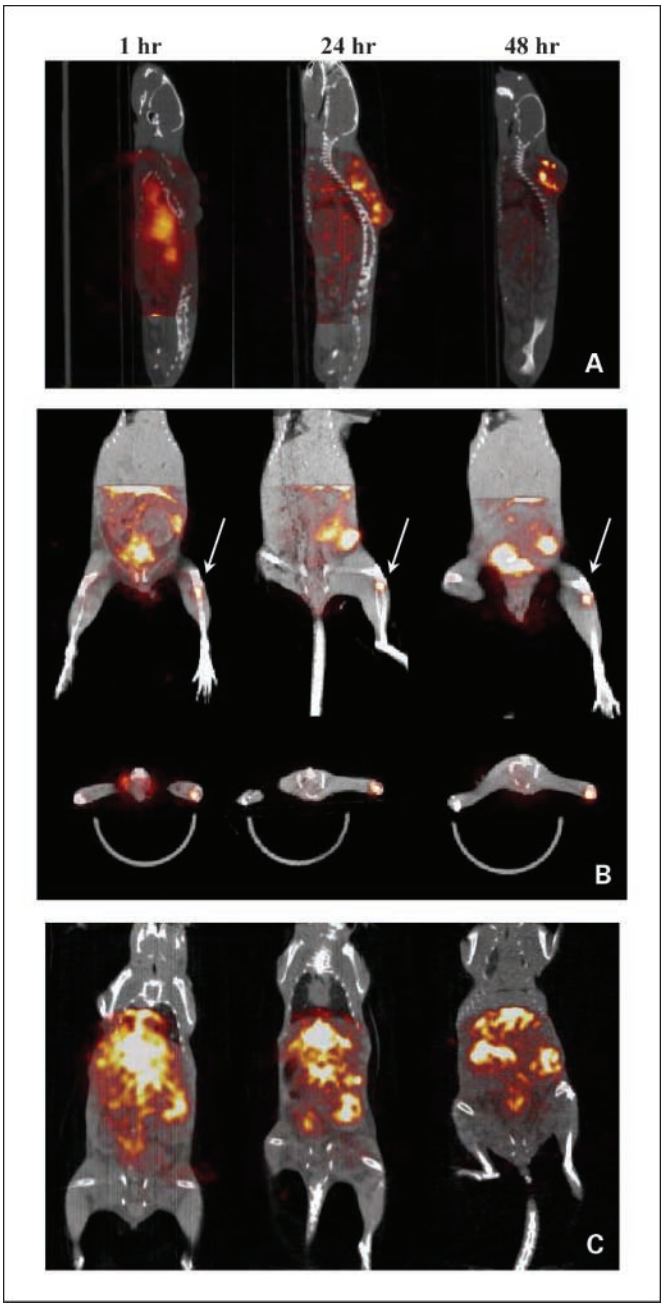

Fig. 4. SPECT/CT imaging of *neu*-N mice (*A*) 18 d after s.c. injection of 1×10^5 NT2.5 cells in the dorsal fat pad and (*B* and *C*) 25 d after left ventricular injection of 1×10^5 NT2.5 cells. *A,* appearance of antibody uptake in the s.c. tumors 1, 24, and 48 h following i.v. injection of 200 μCi ^{111}In-labeled 7.16.4. Tumor localization was only evident 24 h following ^{111}In-7.16.4 injection. *B,* focal uptake near the left femoral-tibial joint was revealed 1 h following ^{111}In-7.16.4 injection and was consistently discernable at 24 and 48 h (*white arrows*) postinjection. Both coronal and transverse views are presented. *C,* persistent accumulation of ^{111}In-7.16.4 was also observed at 1, 24, and 48 h postinjection in liver, spleen, and a flank metastasis in the peritoneal cavity.

PET scan was able to locate the metastases within the skeleton, which are associated with active bone remodeling. Here, two metastatic foci can be identified in the spine. Similarly, multiple sites of increased [^{18}F]FDG uptake can be observed within the axial spine (Fig. 3B, *arrowheads*), indicating locally active tumor metabolism. Diffusion-weighted MRI revealed metastatic cell infiltration around the regions of the bone marrow (Fig. 3C). Multiple tumor foci are visible in a series of contiguous (0.8-mm-thick) slices with tumors (areas with higher diffusion rate) emanating from marrow spaces in both femurs (*slices 2*, *3*, and *4*; *broken line circle*) and vertebral bodies (*slices 4* and *5*, *rectangle*; *slices 6* and *7*, *circle*). Small-animal SPECT/CT imaging of this metastasis model by using ^{111}In-labeled anti-rat HER-2/*neu* mAb (7.16.4) is shown in Fig. 4. A series of small-animal SPECT/CT images at 1, 24, and 48 hours following ^{111}In-7.16.4 injection shows localization of ^{111}In-7.16.4 to a s.c. tumor. At 1 hour after ^{111}In-7.16.4 injection, little tumor localization can be visualized, whereas only by 24 and 48 hours, s.c. localization of ^{111}In-7.16.4 became evident due to slow localization of antibody to the tumor. Localization of ^{111}In-7.16.4 to normal organs expressing rat HER-2/*neu* cannot be detected directly by small-animal SPECT/CT probably because the expression level is too low compared with tumor. In contrast to the localization kinetics observed for the s.c. tumor, increased signal intensity at a focal point in the distal femur near the femoral-tibial joint can be seen at 1 hour following ^{111}In-7.16.4 injection (Fig. 4B). The same focal point was detected at 24 and 48 hours following ^{111}In-7.16.4 injection, which suggests rapid access to micrometastases by ^{111}In-7.16.4 compared with s.c. tumors. Quantification of the focal uptake in the femur-tibial joint showed that the 1-hour uptake level was approximately the same as that at 48 hours. Due to the limited field-of-view of the SPECT camera, imaging of liver and spleen were done in a separate mouse (Fig. 4C). All imaged metastatic foci were confirmed by necropsy and histopathology.

Histopathology of breast cancer metastasis. H&E staining of metastatic tumor in various tissues following left cardiac ventricular injection is shown in Fig. 5. Invasion of the marrow in the distal femur by tumor cells is evident. Osteolysis of the trabecular bone, commonly observed in breast cancer bone metastasis, can be seen in an enlarged area near the femoral-tibial joint (Fig. 5A). Disseminated tumor cells can also been seen to invade and cause lysis of vertebral bone (Fig. 5B) and impinge on the spinal cord, which may have led to hind limb paralysis. Widespread liver metastases were also confirmed with histopathologic staining of disease-laden liver (Fig. 5C). Expression of HER-2/*neu* on metastatic tumor cells in the area near the femoral-tibial joint was confirmed by flow cytometry of the cultured cells collected from bone marrow (Fig. 5D).

Discussion

In this study, we describe an immunocompetent transgenic mouse model of metastatic breast cancer and provide small-animal imaging and histopathologic characterization of this model. Metastatic lesions in the bone marrow, liver, and spleen were detected using small-animal MRI, small-animal PET, or small-animal SPECT/CT. Commonly used bioluminescence imaging of metastatic disease was unsuccessful in immunocompetent *neu*-N mice probably because metastatic seeding of luciferase-transfected NT2.5 cells did not occur due to immune rejection of tumor cells. Such seeding occurred, however, in an immunodeficient nude mouse model, and bioluminescence imaging was shown in the nude mouse model. Longitudinal imaging with small-animal SPECT/CT

in the model provided convincing evidence that radiolabeled antibody could quickly reach and bind to metastatic cells in the bone marrow. This immunotolerant mouse model with multiorgan metastases provides a clinically relevant animal model for better evaluation of immunotherapy as well as feasible imaging modalities to monitor disease progression following therapy.

In vivo molecular imaging of key tumor properties along the pathways of cancer mutation and progression have been intensively researched, such as apoptosis (25), hypoxia and angiogenesis (26), gene expression and regulation (27, 28), metabolism (29), and, more recently, host tumor microenvironment interaction (30, 31). Whole-body imaging of metastatic progression has also been possible due to the

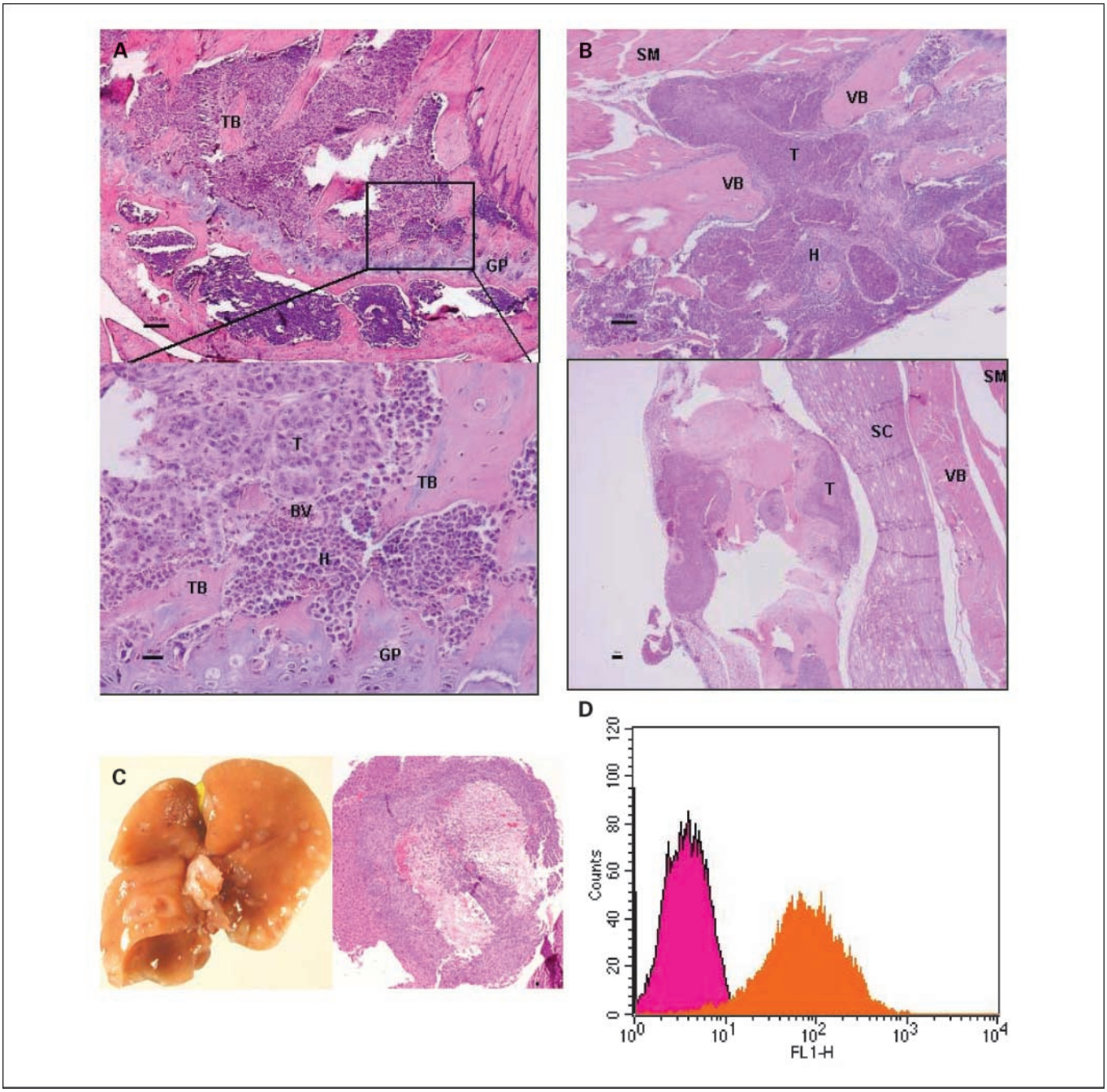

Fig. 5. Histopathologic staining of *neu*-N mouse organs following left cardiac ventricular injection. The same mouse as seen on MRI was sacrificed. Then, femur, spine, and liver were harvested for histopathologic staining. *A,* invasion of distal femur near the femoral-tibial joint by tumor cells is evident. Lysis of the trabecular bone can be seen in enlarged area near the femoral-tibial joint. *B,* disseminated tumor cells invaded and lysed vertebral bone and further intruded into the skeletal muscle. Invasion of metastatic tumor cells can also been seen impinging on the spinal cord. BV, blood vessel; GP, growth plate; H, hematopoietic cells; SC, spinal cord; SM, skeletal muscle; T, tumor cells; TB, trabecular bone; VB, vertebral bone. Black bar, 100 μm. *C,* the liver was infiltrated by numerous metastatic tumor foci in the liver parenchyma. *D,* flow cytometric analysis of HER-2/*neu* expression on cells harvested from the distal femur near femoral-tibial joint of *neu*-N mouse that received NT2.5 cells; NT2.5 cells without the primary antibody are also shown as control.

development of novel bioluminescence and fluorescent imaging techniques (12, 15). Nevertheless, the complex interaction between metastatic invasion and the host immune system has not been completely studied, although disruption of normal tissue architecture by metastatic cells and the ability/inability of the host immune system to respond is believed to be critical to our understanding of metastasis (32). Moreover, numerous immune-mediated cancer treatments have shown that immunotolerance, the inability of the host immune system to recognize and eradicate self-antigens expressed on tumors, can be further aggravated by the tumor induced highly suppressive immune microenvironment containing a complex network of cytokines and various immunosuppressive cells, such as T regulatory cells (33, 34), natural killer T cells (35), myeloid suppressor cells (36, 37), and tumor-associated macrophages (38). A metastatic immunotolerant mouse model can, therefore, provide better prediction of clinical outcomes for novel immunotherapies.

Metastatic mouse models induced based on transplantation of green fluorescent protein, luciferase, or quantum dot–labeled cancer cells are widely used in evaluation of novel treatments of metastasis. The expression of foreign antigens in these cancer cells, however, can elicit immunogenic responses in immunocompetent hosts that might not only affect the progression of disseminated disease but also cause undesirable immune reactions in evaluating immune-based treatments. In fact, green fluorescent protein has been used in an adjuvant setting to augment tumor-specific T cells (39). Noninvasive radiological imaging modalities, more easily translated into clinical practice, are therefore more suitable for monitoring treatment efficacy of immunotherapies in preclinical studies. Small-animal imaging modalities such as small-animal PET, small-animal SPECT, and MRI have already been applied to tracking immune cells in cancer therapies, such as T lymphocytes (40, 41) and dendritic cells (42). *In vivo* monitoring of the response of metastasis to T lymphocytes and the possible induction of anergy in these T cells will be of great interest and can now be possible with the use of such immunotolerant metastatic models.

In using radiolabeled antibody imaging to evaluate the pharmacokinetics of targeting metastatic disease or to monitor disease progression, the possible effect of the antibody itself on disease progression must be considered. In these imaging studies, the protein dose of antibody used for imaging was substantially below the levels known to lead to therapeutic effects (43).

Although left cardiac ventricular injection is effective and has been previously used to induce metastases, the metastatic cells thus generated probably do not accurately model spontaneous metastases. Even in an immunotolerant model, tumor cells introduced by left cardiac injection have not undergone the initial selection of intravascular invasion. Orthotopic implantation of tumor cells followed by surgical resection of the primary tumor can lead to spontaneous metastasis many days later (10). More recently, many efforts have been made to generate genetic mouse tumor models that have the ability of spontaneously metastasizing to different organs (44). We believe that the small-animal imaging modalities described in this study will also be useful for the monitoring of metastatic progression and response to therapy in these models.

Disclosure of Potential Conflicts of Interest

No potential conflicts of interest were disclosed.

References

1. American Cancer Society. Cancer facts and figures 2008; Atlanta (GA): American Cancer Society, Inc.; 2008. p. 17.
2. Weigelt B, Peterse JL, van't Veer LJ. Breast cancer metastasis: markers and models. Nat Rev Cancer 2005;5:591–602.
3. Lee YT. NM Breast-carcinoma—pattern of metastasis at autopsy. J Surg Oncol 1983;23:175–80.
4. Guy CT, Webster MA, Schaller M, Parsons TJ, Cardiff RD, Muller WJ. Expression of the Neu protooncogene in the mammary epithelium of transgenic mice induces metastatic disease. Proc Natl Acad Sci U S A 1992;89:10578–82.
5. Guy CT, Cardiff RD, Muller WJ. Induction of mammary-tumors by expression of polyomavirus middle T-oncogene—a transgenic mouse model for metastatic disease. Mol Cell Biol 1992;12:954–61.
6. Lin SCJ, Lee KF, Nikitin AY, et al. Somatic mutation of p53 leads to estrogen receptor α-positive and -negative mouse mammary tumors with high frequency of metastasis. Cancer Res 2004;64:3525–32.
7. Siegel PM, Shu WP, Cardiff RD, Muller WJ, Massague J. Transforming growth factor β signaling impairs Neu-induced mammary tumorigenesis while promoting pulmonary metastasis. Proc Natl Acad Sci U S A 2003;100:8430–5.
8. Rosol TJ, Tannehill-Gregg SH, Leroy BE, Mandl S, Contag CH. Animal models of bone metastasis. Cancer 2003;97:748–57.
9. Kuperwasser C, Dessain S, Bierbaum BE, et al. A mouse mode of human breast cancer metastasis to human bone. Cancer Res 2005;65:6130–8.
10. Morikawa K, Walker SM, Jessup JM, Fidler IJ. *In vivo* selection of highly metastatic cells from surgical specimens of different primary human colon carcinomas implanted into nude mice. Cancer Res 1988;48:1943–8.
11. Hoffman RM. Orthotopic metastatic mouse models for anticancer drug discovery and evaluation: a bridge to the clinic. Invest New Drugs 1999;17:343–59.
12. Kang YB, Siegel PM, Shu WP, et al. A multigenic program mediating breast cancer metastasis to bone. Cancer Cell 2003;3:537–49.
13. Dunn GP, Bruce AT, Ikeda H, Old LJ, Schreiber RD. Cancer immunoediting: from immunosurveillance to tumor escape. Nat Immunol 2002;3:991–8.
14. Minn AJ, Kang YB, Serganova I, et al. Distinct organ-specific metastatic potential of individual breast cancer cells and primary tumors. J Clin Invest 2005;115:44–55.
15. Hoffman RM. The multiple uses of fluorescent proteins to visualize cancer *in vivo*. Nat Rev Cancer 2005;5:796–806.
16. Andrechek ER, Muller WJ. Tyrosine kinase signalling in breast cancer—tyrosine kinase-mediated signal transduction in transgenic mouse models of human breast cancer. Breast Cancer Res 2000;2:211–6.
17. Chan R, Muller WJ, Siegel PM. Oncogenic activating mutations in the neu/erbB-2 oncogene are involved in the induction of mammary tumors. Ann N Y Acad Sci 1999;889:45–51.
18. Reilly RT, Gottlieb MBC, Ercolini AM, et al. HER-2/neu is a tumor rejection target in tolerized HER-2/neu transgenic mice. Cancer Res 2000;60:3569–76.
19. Machiels JPH, Reilly RT, Emens LA, et al. Cyclophosphamide, doxorubicin, and paclitaxel enhance the antitumor immune response of granulocyte/macrophage-colony stimulating factor-secreting whole-cell vaccines in HER-2/neu tolerized mice. Cancer Res 2001;61:3689–97.
20. Ercolini AM, Ladle BH, Manning EA, et al. Recruitment of latent pools of high-avidity CD8(+) T cells to the antitumor immune response. J Exp Med 2005;201:1591–602.
21. Abbey CK, Borowsky AD, McGoldrick ET, et al. *In vivo* positron of progression-emission tomography imaging of progression and transformation in model of mammary neoplasia. Proc Natl Acad Sci U S A 2004;101:11438–43.
22. Artemov D, Mori N, Ravi R, Bhujwalla ZM. Magnetic resonance molecular imaging of the HER-2/neu receptor. Cancer Res 2003;63:2723–7.
23. Ballangrud AM, Yang WH, Charlton DE, et al. Response of LNCaP spheroids after treatment with an α-particle emitter (213Bi)-labeled anti-prostate-specific membrane antigen antibody (J591). Cancer Res 2001;61:2008–14.
24. Arguello F, Baggs RB, Frantz CN. A murine model of experimental metastasis to bone and bone-marrow. Cancer Res 1988;48:6876–81.
25. Petrovsky A, Schellenberger E, Josephson L, et al. Near-infrared fluorescent imaging of tumor apoptosis. Cancer Res 2003;63:1936–42.
26. Serganova I, Doubrovin M, Vider J, et al. Molecular

imaging of temporal dynamics and spatial heterogeneity of hypoxia-inducible factor-1 signal transduction activity in tumors in living mice. Cancer Res 2004;64:6101–8.

27. Doubrovin M, Ponomarev V, Beresten T, et al. Imaging transcriptional regulation of p53-dependent genes with positron emission tomography *in vivo*. Proc Natl Acad Sci U S A 2001;98:9300–5.

28. Zhang GJ, Safran M, Wei WY, et al. Bioluminescent imaging of Cdk2 inhibition *in vivo*. Nat Med 2004;10:643–8.

29. Golman K, in't Zandt R, Lerche M, Pehrson R, Ardenkjaer-Larsen JH. Metabolic imaging by hyperpolarized C-13 magnetic resonance imaging for *in vivo* tumor diagnosis. Cancer Res 2006;66:10855–60.

30. Acuff HB, Carter KJ, Fingleton B, et al. Matrix metalloproteinase-9 from bone marrow-derived cells contributes to survival but not growth of tumor cells in the lung microenvironment. Cancer Res 2006;66:259–66.

31. van der Pluijm G, Que I, Sijmons B, et al. Interference with the microenvironmental support impairs the *de novo* formation of bone metastases *in vivo*. Cancer Res 2005;65:7682–90.

32. Pardoll D. Does the immune system see tumors as foreign or self? Annu Rev Immunol 2003;21:807–39.

33. Sakaguchi S, Sakaguchi N, Shimizu J, et al. Immunologic tolerance maintained by CD25(+) CD4(+) regulatory T cells: their common role in controlling autoimmunity, tumor immunity, and transplantation tolerance. Immunol Rev 2001;182:18–32.

34. Curiel TJ, Coukos G, Zou LH, et al. Specific recruitment of regulatory T cells in ovarian carcinoma fosters immune privilege and predicts reduced survival. Nat Med 2004;10:942–9.

35. Terabe M, Matsui S, Noben-Trauth N, et al. NKT cell-mediated repression of tumor immunosurveillance by IL-13 and the IL-4R-STAT6 pathway. Nat Immunol 2000;1:515–20.

36. Serafini P, Carbley R, Noonan KA, Tan G, Bronte V, Borrello I. High-dose granulocyte-macrophage colony-stimulating factor-producing vaccines impair the immune response through the recruitment of myeloid suppressor cells. Cancer Res 2004;64:6337–43.

37. Huang B, Pan PY, Li QS, et al. Gr-1(+)CD115(+) immature myeloid suppressor cells mediate the development of tumor-induced T regulatory cells and T-cell anergy in tumor-bearing host. Cancer Res 2006;66:1123–31.

38. Sica A, Schioppa T, Mantovani A, Allavena P. Tumour-associated macrophages are a distinct M2 polarised population promoting tumour progression: Potential targets of anti-cancer therapy. Eur J Cancer 2006;42:717–27.

39. Re F, Srinivasan R, Igarashi T, Marincola F, Childs R. Green fluorescent protein expression in dendritic cells enhances their immunogenicity and elicits specific cytotoxic T-cell responses in humans. Exp Hematol 2004;32:210–7.

40. Kircher MF, Allport JR, Graves EE, et al. *In vivo* high resolution three-dimensional imaging of antigen-specific cytotoxic T-lymphocyte trafficking to tumors. Cancer Res 2003;63:6838–46.

41. Koehne G, Doubrovin M, Doubrovina E, et al. Serial *in vivo* imaging of the targeted migration of human HSV-TK-transduced antigen-specific lymphocytes. Nat Biotechnol 2003;21:405–13.

42. de Vries IJM, Lesterhuis WJ, Barentsz JO, et al. Magnetic resonance tracking of dendritic cells in melanoma patients for monitoring of cellular therapy. Nat Biotechnol 2005;23:1407–13.

43. Song H, Shahverdi K, Huso DL, et al. α-Particle emitter labeled monoclonal antibody [213Bi-7.16.4] (anti-HER-2/neu) targeting of breast cancer metastases in the neuN HER-2/neu transgenic mouse model. Cancer Res 2008;68:3873–80.

44. Nguyen DX, Massague J Genetic determinants of cancer metastasis. Nat Rev Genet 2007;8:341–52.